Supplementary Materials for

Frequency-dependent seismic radiation process of the 2024 Noto Peninsula earthquake from teleseismic P-wave back-projection

K. Tarumi[1,*] and K. Yoshizawa[1,2]

[1] Department of Natural History Sciences, Graduate School of Science, Hokkaido University, Sapporo 060-0810, Japan

[2]Department of Earth & Planetary Sciences, Faculty of Science, Hokkaido University, Sapporo 060-0810, Japan.

[*]Corresponding author: tarumi.kotaro.jp@gmail.com

This is a preprint that is submitted to EarthArXiv. The original manuscript has been submitted to Earth and Planetary Science Letters.

Highlights

Frequency-dependent seismic radiation process of the 2024 Noto Peninsula earthquake from teleseismic P-wave back-projection

Kotaro Tarumi, Kazunori Yoshizawa

- The source process of the 2024 Noto earthquake is imaged by P-wave back-projection.
- Multi-frequency back-projection images reveal complex fault rupture sequences.
- Main source rupture propagates bilaterally toward inland and offshore regions.
- High-frequency P-waves are radiated before the rapid main rupture propagation.
- Frequency-dependent P-wave radiations reflect the effects of complex fault geometry.

Frequency-dependent seismic radiation process of the 2024 Noto Peninsula earthquake from teleseismic P-wave back-projection

Kotaro Tarumi[a], Kazunori Yoshizawa[a,b]

[a]*Department of Natural History Sciences, Graduate School of Science, Hokkaido University, Sapporo 060-0810, Japan., Sapporo, 060-0810, Japan*
[b]*Department of Earth and Planetary Sciences, Faculty of Science, Hokkaido University, Sapporo, 060-0810, Japan*

Abstract

A large devastating earthquake of Mw 7.5 struck the Noto Peninsula, Japan, on January 1st, 2024. Persistent seismic swarms have continued around the hypocenter since 2020, likely driven by crustal fluids migrating upward from the lower crust. In this study, we investigated the frequency-dependent seismic radiation process using multi-frequency teleseismic P-wave back projection. The resulting source process reveals complex frequency-dependent behavior, which can be divided into four episodes. The initial episode lasts 15–20 s, characterized by high-frequency energy preceding low-frequency radiation. The second episode is marked by intense high-frequency P-wave emission with the absence of low-frequency signals. Then, intensive low-frequency P-waves are radiated from the source region, with ruptures propagating bilaterally from the hypocentral area toward the southwestern inland (third episode) and northeastern offshore (fourth episode) regions. The fluid-rich condition near the hypocenter likely plays an important role in controlling fault rupture, contributing to the observed complex rupture processes. The intricate fault geometry around the source region may have also contributed to the characteristic frequency-dependence of P-wave radiation during this earthquake.

Keywords: 2024 Noto Earthquake, P-wave radiation, back projection, source process, crustal fluid, fault geometry

1. Introduction

On January 1st, 2024, a large and devastating earthquake with a moment magnitude (Mw) of 7.5 (Dziewonski et al., 1981; Ekström et al., 2012) occurred in the Noto Peninsula in Japan, causing widespread destruction and collapse of numerous buildings, with over 400 casualties reported by the Fire and Disaster Management Agency (FDMA; FDMA (2024)) of Japan. Several locations recorded the maximum seismic intensity of 7, the highest on the Japan Meteorological Agency (JMA) scale, with the Noto Peninsula experiencing strong ground motion and coastal uplift. This earthquake also generated a tsunami with a maximum height of 5 meters, which was observed not only around the peninsula but also in Korea, North Korea, and Russia (Fujii and Satake, 2024; Mizutani et al., 2024).

This destructive earthquake has been identified as a thrust fault based on local JMA (2024a) and global seismic waveform analyses (e.g., global CMT; Dziewonski et al., 1981; Ekström et al., 2012) (Figure 1). The aftershock distribution provided by JMA indicates that the source fault length extends to

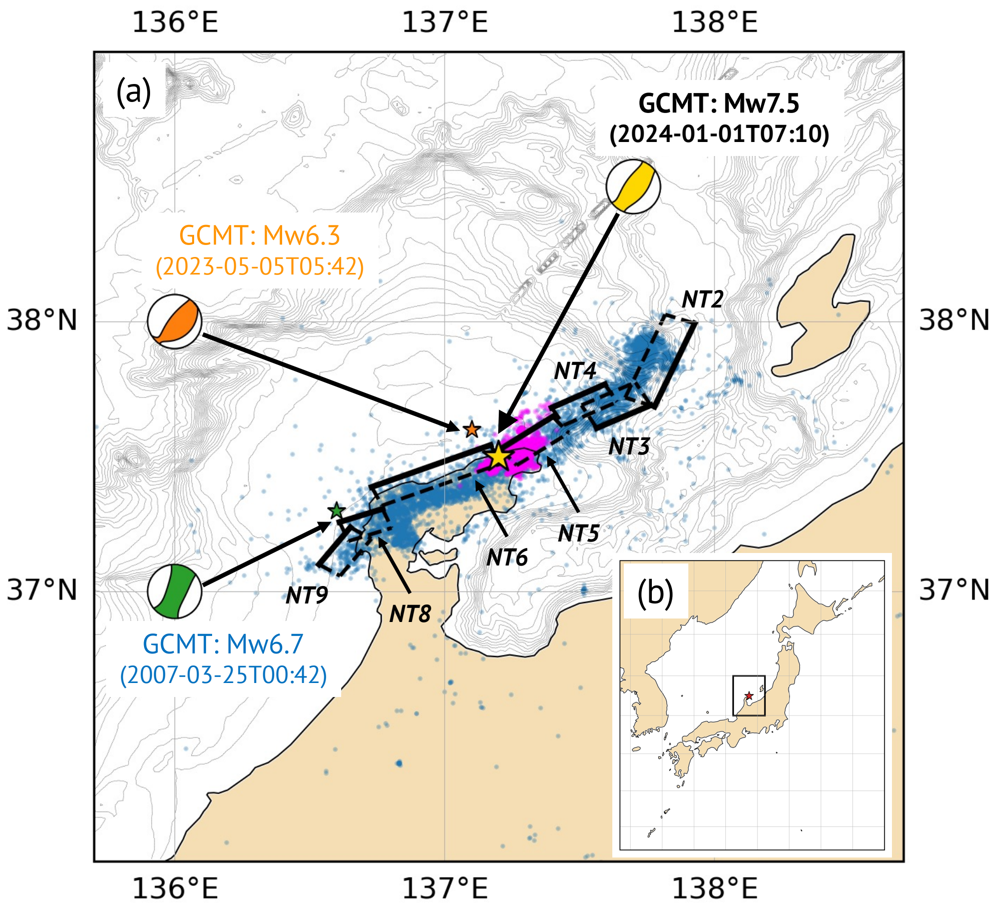

Figure 1: (a) The locations of the Mw 7.5 2024 Noto Peninsula Earthquake on January 1st, 2024, and its aftershocks as well as recent large earthquakes in our study area. All origin times are in UTC. The yellow star and focal mechanism represent the epicenter of the Mw 7.5 event on January 1st, 2024, and its focal mechanism from Global CMT (Dziewonski et al., 1981; Ekström et al., 2012). Blue dots indicate the distribution of aftershocks until January 14th, 2024 (JMA, 2024a). The other two stars and corresponding focal mechanisms denote past large events in 2007 and 2023. Magenta dots represent the preceding seismic events (since November 2020) leading to the Mw 7.5 mainshock, as reported by Yoshida et al. (2023a). Seven black rectangles exhibit the fault models from the Japan Sea earthquake and tsunami project (JSPJ) (MEXT, 2013), NT2, NT3, NT4, NT5, NT6, NT8, and NT9, in which solid black lines indicate the top of each fault. Inset (b) displays a broader-scale map indicating the location of the study area. The black rectangle encompasses the area shown in (a), where the red star marks the epicenter of the Mw 7.5 main event reported by USGS (USGS, 2024).

about 150 km (JMA, 2024a) (gray dots in Figure 1), which is more extensive than other inland earthquakes of similar magnitude in Japan. In addition, the fault geometry appears complex; the inland region mainly dips toward the southeast, while the offshore region may involve northwest-dipping faults. Several studies have analyzed the seismic source process using the seismic records from near-field and teleseismic stations, geodetic data (e.g., GNSS), and local tsunami waveforms (e.g., Fujii and Satake, 2024; Okuwaki et al., 2024; Mizutani et al., 2024; Kutschera et al., 2024; Ma et al., 2024; Xu et al., 2024). Many of these studies have identified two large-slip areas in the western inland and eastern offshore regions of the Noto Peninsula, resulting from bilateral rupture propagation from the hypocentral region toward these slip areas.

Seismic swarms have occurred near the hypocenter of the Mw 7.5 event since November 2020 (e.g., Amezawa et al., 2023; Nishimura et al., 2023; Yoshida et al., 2023b), likely driven by the upward migration of fluid Nishimura et al. (2023). The presence of high pore pressure may be related to the complex fault rupture processes, such as super-shear rupture (Pampillón et al., 2023). Additionally, fluids can effectively weaken the fault cohesion, possibly causing the fault to slip more easily (Gabriel et al., 2012; Madden et al., 2022). Earlier works employing seismic data (Okuwaki et al., 2024; Kutschera et al., 2024; Ma et al., 2024; Xu et al., 2024) suggest that the complex source process within the intricate fault network may be controlled by upward-migrating crustal fluids. Interestingly, Kutschera et al. (2024) argued that the fault rupture may have been renucleated in the hypocentral region 20 s after the origin time (2024-01-01T07:10 UTC), which may result from the fault weakening by the high pore pressure. Meanwhile, Yoshida et al. (2024) relocated the aftershock distribution and discussed the relationships among the local seismicity, the Mw 7.5 earthquake, hidden faults, and the upward migrating fluid. Investigations into this devastating Mw 7.5 earthquake are crucial for understanding the influence of the crustal fluids on fault behavior.

The frequency dependence of the rupture process remains a controversial topic in seismic source studies (Koper et al., 2011; Ishii, 2011; Koper et al., 2012; Yagi et al., 2012). Low-frequency signals are particularly useful for imaging the macroscopic rupture process, as they are sensitive to regions of large slip. High-frequency seismic energy radiation, on the one hand, is essential for understanding the complexities of the seismic source process (e.g., Okuwaki et al., 2018). Previous studies including theoretical analysis, laboratory experiment, and seismic waveform analysis have shown that high-frequency P-waves can reflect abrupt changes in slip and/or rupture velocity on the fault surface (e.g., Bernard and Madariaga, 1984; Spudich and Frazer, 1984; Beresnev, 2017), as well as the fault roughness, such as the fault barriers and branching (e.g., Adda-Bedia and Madariaga, 2008; Uchide et al., 2013; Bruhat et al., 2016; Okuwaki and Yagi, 2017). Furthermore, many classical studies suggest that high-frequency radiation coincides with the termination of fault rupture or slip, a phenomenon known as the stopping phase (e.g., Savage, 1965; Bernard and Madariaga, 1984). Thus, incorporating both high-and low-frequency teleseismic signals enables a comprehensive understanding of earthquake rupture process across a broad range of frequencies.

For the Noto peninsula earthquake, Okuwaki et al. (2024) and Kutschera et al. (2024) highlighted the complexities of the fault geometry through sophisticated teleseismic waveform inversion, which may have contributed to the generation of high-frequency seismic waves. In the Mw 7.9 Türkey-Kahramanmaras earthquake, Mai et al. (2023) used teleseismic P-wave back-projection in two frequency bands (0.1–0.5 Hz; 0.5–1.0 Hz) to detect the stopping phase, which has proven useful for investigating the mechanisms of small earthquakes (e.g., Imanishi and Takeo, 1998, 2002), resulting from abrupt rupture termination. High-frequency seismic waves are crucial for understanding complex seismic source processes, making frequency-dependent radiation analysis valuable in elucidating the mechanisms of this devastating earthquake.

In this study, we investigate frequency-dependent seismic-wave radiation processes using the back-projection (BP) of teleseismic P-waves across multiple frequency ranges (0.03–0.3 Hz; 0.05–0.5 Hz; 0.1–1.0 Hz; 0.3–2.0 Hz). By analyzing the time series of BP images for different frequency ranges, we explore the relationship between high-frequency seismic wave radiation and the large-scale rupture process characterized by lower-frequency P-wave radiation.

2. Data and Method

This earthquake is listed as two separate events in the earthquake catalog of the Japan Meteorological Agency (JMA, 2024a); M_{jma} 5.9 and M_{jma} 7.6. However, for the purpose of our analysis, we treat these two earthquakes as a single Mw 7.5 event.

2.1. Multi-frequency Teleseismic P-wave

We used three-component seismograms at global seismic stations downloaded from the IRIS Data Management Center. Prior to waveform processing, we removed the instrument response from the raw data, converted them to displacement waveforms, and resampled them at 0.1 s intervals.

Our data selection method generally follows Tarumi and Yoshizawa (2023). First, we selected seismic stations located between 30° and 95° from the epicenter, as our target phase is the teleseismic P-wave. Second, we grouped displacement waveforms based on a cross-correlation coefficient (CC) greater than 0.7 and corrected the travel time using the lag time to account for 3-D structural effects. In this process, the time window was set to 15 s before and 15 s after the theoretical P-wave arrival times based on the AK135 model. Finally, we retained the group containing the largest number of waveforms for the back-projection analysis.

To estimate the frequency-dependent seismic radiation, we applied multiple bandpass filters to three-component seismograms with multiple frequency ranges: 0.03-0.3 Hz, 0.05-0.5 Hz, 0.1-1.0 Hz, and 0.3-2.0 Hz. The prescribed waveform-selection steps were conducted in each frequency range. Figure 2 shows an example of our teleseismic dataset for the lowest-frequency range, 0.03-0.3 Hz, while Figures S1-S3 in Supplementary Material display the datasets for the other frequency bands. For all frequency bands used in this study, our teleseismic datasets exhibit good azimuthal coverage (e.g., Figure 2), ensuring high resolution in the back-projection analysis (e.g., Okuwaki et al., 2014; Kiser and Ishii, 2016).

2.2. Back Projection with LQT coordinate system

Seismic back-projection (BP) analysis time-reverses observed seismograms to the source time and locations from which the target seismic phase is radiated. BP was originally developed to image the rupture evolution (Ishii et al., 2005, 2007) and has been widely used in seismic source studies involving the detection of aftershocks hidden in large earthquakes (e.g., Kiser and Ishii, 2013a), the estimation of tsunami-generating regions (Mizutani and Yomogida, 2022), and tracking the eruption sequence on the 2022 Tonga eruption (Tarumi and Yoshizawa, 2023).

BP analysis has generally been performed using the vertical-component seismograms (e.g., Ishii et al., 2007; Kiser and Ishii, 2013b; Xu et al., 2009; Okuwaki et al., 2014; Kehoe et al., 2019; Tarumi and Yoshizawa, 2023), as teleseismic P-waves are primarily recorded in the vertical component. However, the particle motion of teleseismic P-waves is inclined, involving some amount of signals in the horizontal (radial) component, even at epicentral

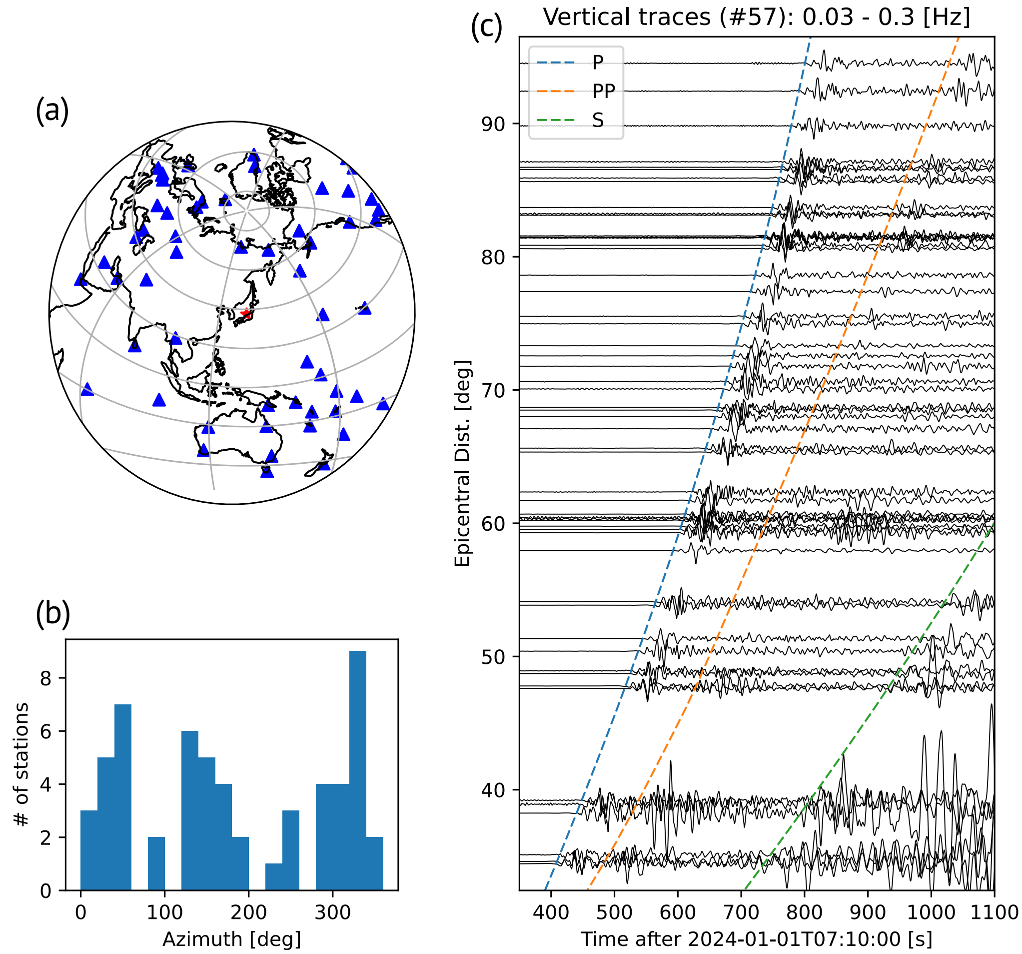

Figure 2: Teleseismic waveform dataset used for the BP analysis with a frequency range of 0.03-0.3 Hz. (a) Map of the stations used. The red and blue triangles indicate the hypocenter and seismic stations, respectively. (b) Histogram of the azimuths from the source to the stations. (c) Vertical-component seismograms, scaled by the maximum amplitude of direct P phase. The blue, orange, and green lines represent the travel-time curves for P, PP, and S waves, respectively.

distances of around 90°. This inclination increases at stations closer to the source. Thus, to consider the total amplitude of P-waves, it is preferable to incorporate the two horizontal components in addition to the vertical component. In this study, we employ the LQT coordinate system (also known as the ray-coordinate system) (Vinnik, 1977) to implement the BP analysis (hereafter referred to as the LQT-BP method). Figure S4 illustrates the ray-coordinate system. This new coordinate system, commonly used in receiver function studies (e.g., Kind and Yuan, 2011), is derived by rotating the three-component seismograms into the direction of the P-wave incidence (L), the perpendicular direction to the L-component (Q), and the transverse direction (T) (Vinnik, 1977) (Figure S4). The use of the LQT system enhances the direct P-wave signal, potentially leading to more refined BP images.

In our BP analyses, we utilized the N-th root stacking method (Rost and Thomas, 2002), which effectively enhances coherent signals. This robust stacking approach has been applied in many previous BP studies (Xu et al., 2009; Honda et al., 2011, 2013; Mizutani and Yomogida, 2022; Tarumi and Yoshizawa, 2023), enabling us to suppress noises and to enhance the BP images for target signals, such as P-waves.

Our LQT-BP analysis can be formulated as follows,

$$L'_j(t, \mathbf{x}_j) = \frac{1}{M} \sum_{i=1}^{M} \mid l_i(t + \tau_{ij}) \mid^{\frac{1}{N}} \cdot \mathrm{sgn}(l_i(t + \tau_{ij})) \tag{1}$$

$$L_j(t, \mathbf{x}_j) = \mid l_j(t) \mid^{N} \cdot \mathrm{sgn}(L'_j(t, \mathbf{x}_j)) \tag{2}$$

where M is the number of stations, τ_{ij} the predicted arrival time between the i-th station and the j-th source grid, l_i an L-component seismogram at the i-th station, $\mathbf{x}_j$ the coordinate point of j-th source grid, and $L_j(t)$ the stack of L-component waveforms at the j-th source grid associated with the total radiation power of seismic waves. In this study, we adopted $N = 4$ for all frequency ranges. Finally, to extract the spatiotemporal radiation intensity $BP(t, \mathbf{x}_j)$, we integrate $L_j(t, \mathbf{x}_j)$ as follows,

$$BP(t, \mathbf{x}_j) = \int_{t-\delta t}^{t+\delta t} L_j(t^{'}, \mathbf{x}_j) dt^{'}, \quad (3)$$

where δt represents an integration interval. In this study, the interval is adaptively defined as half of the averaged period $T^{'}$ for each frequency range, with a minimum δt of 1 second.

The LQT-BP method employed in this study requires both the travel time and the incident angle of the P-wave before stacking (eqs. (1) and (2)). To calculate the theoretical arrival times and incident angles of P-waves, we used a 1-D spherical structure model AK135 (Kennett et al., 1995). Potential source grids are distributed between $-1.5°$ and $+1.5°$ around the epicenter (E137.2, N37.5) at a depth of 10 km, sufficiently covering the potential source region (Figure 1). The source grid interval is set to $0.05°$, except for the highest frequency range (0.3–2.0 Hz), where it is reduced to $0.015°$ to take account of the shorter wavelength.

3. Results

Our BP analysis successfully estimated the frequency-dependent P-wave radiation process. The results are displayed in Figures 3 and 4, as well as in Supplementary Movie S1. Figure 3 presents the multi-frequency BP snapshots at 5-second intervals, with the fault models from the Japan Sea earthquake and tsunami project (JSPJ; MEXT (2013)) superimposed. Figure 4 (a) shows a temporal radiation power of P-waves for each frequency band. Figure 4 (b) displays the contribution of each frequency band, providing a clear view of which frequency bands dominate at each time step during seismic radiation. Figure 5 shows the time evolution of P-wave radiation, projected along the N60°E line, with the projected points indicated in Figure S5.

Across all frequency ranges, the radiation areas cover the JSPJ fault model (black dotted squares in Figures 3). The P-wave radiation extended from the epicenter toward the western inland and eastern offshore regions (Figure 3) and persisted for approximately 44 s, with peak radiations occurring 30-40 s after the origin time (07:10:10 UTC) (Figure 4). The radiation sequence can be divided into four main episodes (Figures 5): [E1] initial radiation near the hypocenter (0–18 s), [E2] intense high-frequency radiation between the initial stage and the subsequent main radiation phases (18–28 s), [E3] strong radiation in the inland region of the Noto Peninsula (25-44 s), and [E4] significant radiation in the eastern offshore region (25-44s). Hereafter, in each episode, relatively higher-frequency P-wave radiations are denoted with a superscript prime (e.g., E1$'$ for higher frequency signals corresponding to the first episode, E1).

The rupture episodes characterized by low-frequency radiation are consistent with previous studies using teleseismic P-waves (Okuwaki et al., 2024; Kutschera et al., 2024; Ma et al., 2024; Xu et al., 2024), which identified a bilateral rupture propagating toward the southwest inland and eastern offshore regions from the hypocenter over approximately 40 s. However, prior to this main bilateral migration, during [E2], high-frequency P-waves (0.1–1.0 Hz and 0.3–2.0 Hz, E2$'$) were radiated intensely from the hypocentral area between 18–25 s, despite the absence of low-frequency energy (Figures 3, 4, and 5), a distinct feature of this Mw 7.5 earthquake.

Figure S6 displays the BP results derived from conventional BP imaging using only the vertical component of P-waves. The LQT-BP results (Figure 3 and 4) resemble those from the traditional BP (Figure S6), but the LQT-BP method slightly enhances the P-wave sources, suggesting that the ray-coordinate system allows us to extract P-wave amplitudes effectively. Still, for the discussion of the source rupture process, the choice of a coordinate system for stacking seismograms seems not to be critical.

3.1. E1: Initial radiation around the hypocenter (0–18 s)

This episode corresponds to the initial rupture stage of the Mw 7.5 earthquake in the hypocentral area. At this initial stage, relatively high-frequency P-wave radiation (0.3–2.0 Hz, E1$'$) is observed preceding the low-frequency

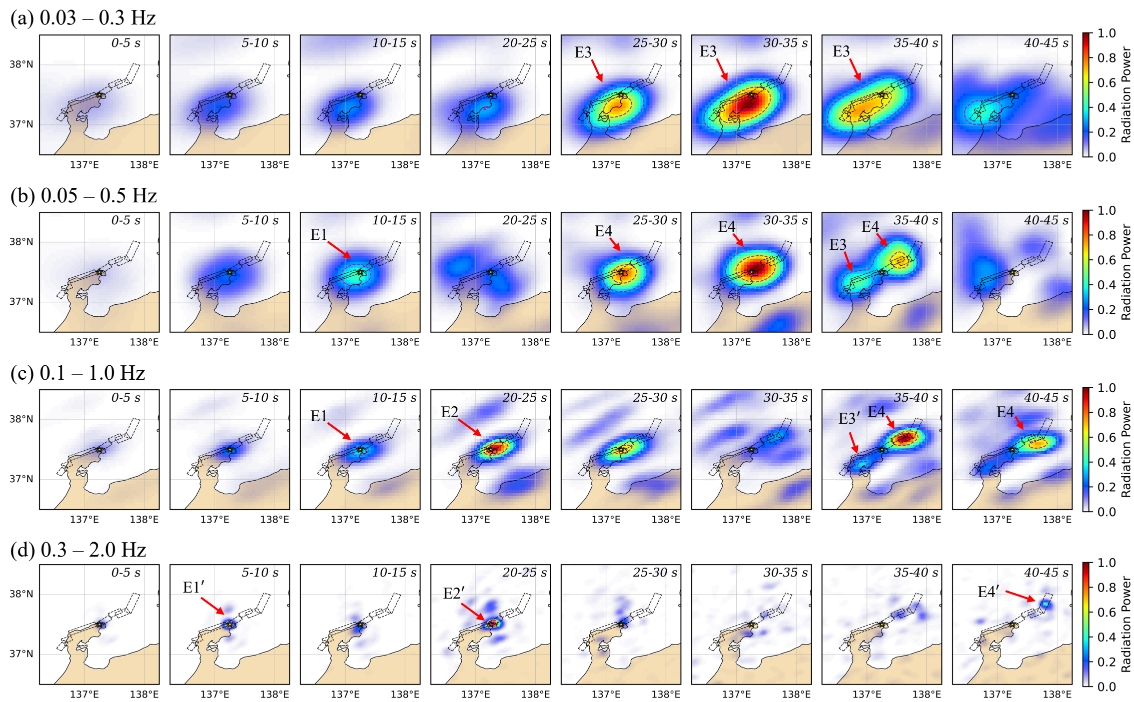

Figure 3: BP snapshots with 5-second intervals for multiple frequency bands: (a) 0.03–0.3 Hz, (b) 0.05–0.5 Hz, (c) 0.1–1.0 Hz, and (d) 0.3–2.0 Hz. Rectangles with black dotted lines represent the fault models from the JSPJ (MEXT, 2013), NT2, NT3, NT4, NT5, NT6, NT8, and NT9, marked in Figure 1. Yellow stars indicate the epicenter of the Mw 7.5 event (USGS, 2024), which occurred at 07:10:10 (UTC). Magenta thin contour lines show radiation intensities at 30 %, 60 %, and 90 %. Radiation power is normalized to the maximum value for each frequency band. The red arrows highlight the locations of notable higher-frequency (HF) radiation (E1′, E2′, E3′, and E4′) and the corresponding lower-frequency radiation (E1, E2, E3, and E4).

component near the hypocenter during the first 0–10 s (Figures 3 (d), 5 (d)). Between 10 and 15 s, the main seismic radiation shifts to the lower-frequency range (0.05-0.5 Hz), which becomes the dominant seismic energy source in this stage. The seismic radiation then fades (Figures 3 (b) and 5 (b)). The early stage of this episode (0–10 s) may be comparable to the initial quiet slip and slow rupture process described by Okuwaki et al. (2024), Ma et al. (2024), and Xu et al. (2024).

3.2. E2: High-frequency radiation lacking low-frequency (18–28 s)

Between 18 and 28 s, intense high-frequency P-waves radiation (0.1–2.0 Hz, $E2'$) emerges from the hypocentral region, while low-frequency P-waves (0.03–0.5 Hz) are notably absent. This frequency-dependent behavior is reflected in the time-dependent radiation power (Figure 4). The highest-frequency P-wave radiation is concentrated around the hypocenter between 18 and 25 s ($E2'$), during which low-frequency radiation temporarily ceases (Figures 3, 4, and 5), creating a hole in the low-frequency radiation. During this gap, the high-frequency component (0.1–2.0 Hz) dominates the total radiation power (Figure 4). This distinct high-frequency radiation may be essential to understanding the rupture process of this Mw 7.5 earthquake, possibly serving as a bridge between the initial stage (E1) and the main rupture stages (E3 and E4).

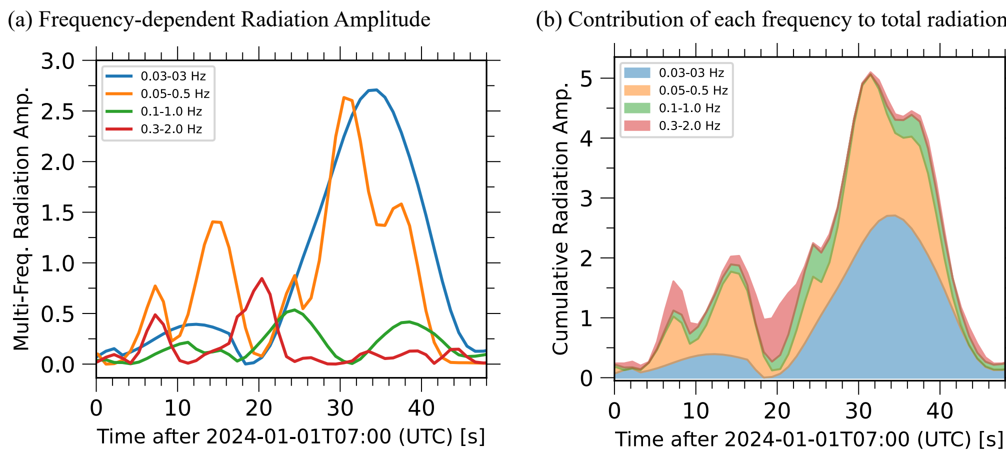

Figure 4: P-wave radiation power as a function of time. (a) Temporal radiation power across multiple frequency bands, with colored lines indicating different frequency ranges: blue (0.03–0.3 Hz), orange (0.05–0.5 Hz), green (0.1–1.0 Hz), and red (0.3–2.0 Hz). (b) Relative contributions of each frequency band to the total radiation power of the four frequency bands. The colored areas correspond to the same frequency bands as in (a).

3.3. E3: Intense radiation in the inland of the Noto Peninsula (25–44 s)

This episode represents one of the most significant stages of seismic radiation, extending across the entire peninsula (Figure 3 (a)). The dominant frequency content of this episode is in the lowest frequency range (0.03-0.3 Hz) of our analysis. The substantial low-frequency radiation propagates toward the southwestern inland areas of the Noto Peninsula from 25 to 44 s (Figure 3 (a)). From 28 s to 40 s, the low-frequency P-wave radiation reaches its peak intensity, representing the most powerful phase of this Mw 7.5 earthquake (Figures 3 and 5). This intense low-frequency radiation may have contributed to the destructive damage in the inland areas of the peninsula. The migration speed of the fault rupture area between 28 and 35 s is estimated to be approximately 3.0 km/s (Figure 5). This stage notably lacks high-frequency signals, but after 40 s, the low-frequency radiation gradually diminishes, accompanied by a weak emission of higher-frequency signals (0.1–1.0 Hz, E3$'$) near the southwestern tip of the peninsula (Figures 3 and 5).

3.4. E4: Intense radiation in the eastern offshore region (25–44 s)

E4 corresponds to intense radiation in the eastern offshore region, primarily within the frequency ranges of 0.05-0.5 Hz and 0.1–1.0 Hz (Figures 3 and 5). During this stage, the P-wave radiation source propagates from the vicinity of the hypocenter toward the eastern offshore region, lasting from 20 to 25 s. The radiation peaks at 30–35 s in the offshore regions, similar to the inland radiation in E3 (Figures 3, 4, and 5), potentially contributing to tsunami generation. The migration speed of the rupture front during this stage is somewhat slower than that in E3, with an estimated speed of less than 3.0 km/s (Figure 5). Around 38 s, this stage abruptly ceases seismic radiation, accompanied by a notable increase in higher-frequency P-wave emissions (E4$'$ in Figures 3, 4, and 5). The location of this frequency transition coincides with the eastern offshore fault (N2) (Figure 3 (c,d)).

4. Discussion

The resultant BP images reveal a notable frequency dependence, indicating significant complexity in the seismic radiation processes of this Mw 7.5 earthquake. These complex processes may be attributed to crustal fluids

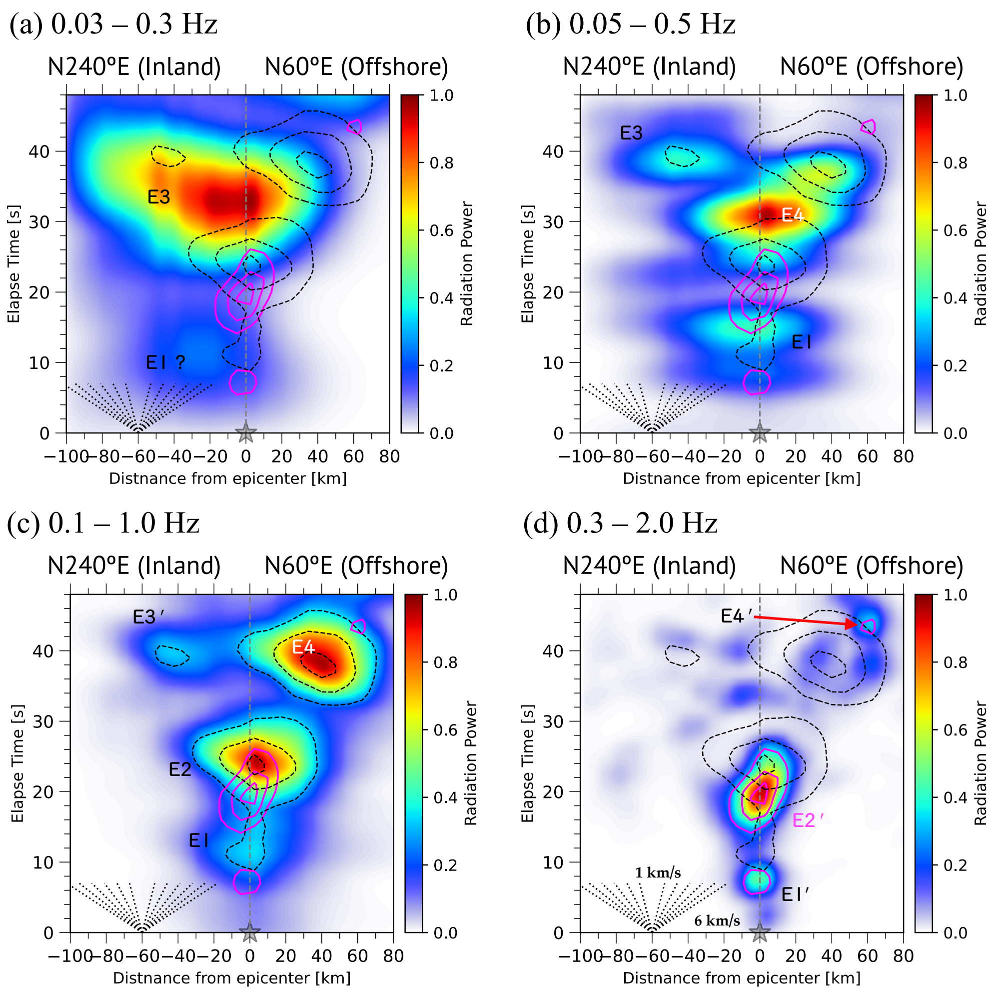

Figure 5: Time evolution of P-wave radiation projected along the N60°E line for multiple frequency bands: (a) 0.03–0.3 Hz, (b) 0.05–0.5 Hz, (c) 0.1–1.0 Hz, (d) 0.3–2.0 Hz. Gray stars represent the epicenter. Vertical dashed lines divide the positive and negative sides in the horizontal axis, corresponding to the northeast offshore and southwest inland parts of the Noto Peninsula, respectively. Dashed lines in the lower left indicate rupture velocities, ranging from 1.0 to 6.0 km/s. E1, E2, E3, and E4 represent the radiation episodes identified in this study. In all panels, black and magenta contour lines indicate 30 %, 60 %, and 90 % of the highest-frequency radiation (black dashed: 0.1–1.0 Hz, magenta solid: 0.3–2.0 Hz).

that have driven long-term seismic swarms in this region since November 2020 (Amezawa et al., 2023). Nishimura et al. (2023) proposed that the upward migration of fluids weakened fault strength, generating the preceding seismic swarms in the Noto Peninsula. Yoshida et al. (2024) suggested that the crustal fluid may have triggered the main rupture process associated with E3 and E4 in this study. Additionally, Nakajima (2022) identified a high Vp/Vs ratio in the in the lower crust beneath the hypocentral area, indicating fluid-rich material. The source region for this destructive event comprises a complex fault system (MEXT, 2013). While the southwestern faults dip toward the southeast, the northeastern offshore region has an opposite dipping direction toward northwest (Figures 1 and 3, and MEXT (2013)), as evidenced by the aftershock distribution (JMA, 2024a). Relocated seismic events also revealed a fault system with multiple hidden faults (Yoshida et al., 2024), suggesting that the hypocentral area likely comprises at least three intersecting faults.

In this section, we first reveal the sources of the prominent highest frequency P-waves (0.03–2.0 Hz), E1$'$, E2$'$, and E4$'$. Such high-frequency P-waves generally reflect complex and smaller-scale fault processes rather than the macroscopic rupture process. Typically, high-frequency seismic signals are generated by rapid changes in rupture and/or slip speed, complex fault branching, and interactions with fault barriers and asperities (e.g., Savage, 1965; Madariaga, 1977; Spudich and Frazer, 1984; Bernard and Madariaga, 1984; Madariaga, 2003; Adda-Bedia and Madariaga, 2008; Beresnev, 2017;

Marty et al., 2019), all of which are essential for unraveling this complex earthquake. Following the clarification of these smaller-scale complexities in seismic radiation, we further discuss the broader frequency-dependent characteristics of the radiation processes derived from our BP analysis.

4.1. E1′: Starting phase of this Earthquake

The first instance of high-frequency radiation, E1′ (Figure 5), likely represents the initiation of the fault rupture process or the starting phase (Madariaga, 1977). At the onset of rupture, substantial energy is required to accelerate the rupture rapidaly as strain energy is released (Madariaga, 1983). E1′ follows the lower-frequency energy (0.05–1.0 Hz) concentrated near the hypocentral region (Figure 5), suggesting that it may be the initial triggering event of this Mw 7.5 earthquake.

Following this initiation phase, the region radiating P-waves does not spread significantly at this stage (Figure 3), which could result from a slower rupture speed (Okuwaki et al., 2024; Ma et al., 2024; Xu et al., 2024). Due to the presence of crustal fluid near the hypocentral region (Nakajima, 2022), the rupture front may not accelerate effectively. This observation supports the discussion of fluid-induced slow rupture initiation, accompanied by high-frequency seismic radiation, as proposed by (Ma et al., 2024).

4.2. E2′: Triggering the low-frequency radiation of E2, E3 and E4

The second event of high-frequency seismic emission (E2′ in Figure 5 (d)) likely reflects a secondary initiation within a doublet event sequence. According to the JMA earthquake catalog (JMA, 2024a), this Mw 7.5 earthquake involves two distinct events of M_{jma} 5.9 (at 16:10:9.54) and M_{jma} 7.6 (at 16:10:22.57), where M_{jma} is JMA's magnitude scale based on observed displacement and/or velocity waveform amplitude (JMA, 2024b). The larger event occurred about 10–15 s after the smaller M_{jma} 5.9 foreshock. The timing of E2$'$ inferred from this study is roughly consistent with the origin time of the larger M_{jma} 7.6 event. Yoshida et al. (2024) relocated the doublets and nearby earthquakes, suggesting that both the M_{jma} 5.9 foreshock and the M_{jma} 7.6 mainshock occurred on the same fault plane. Thus, E2 in our BP results from teleseismic records likely corresponds to the initiation of the larger mainshock in this doublet earthquake.

Crustal fluids, identified by an anomalously high Vp/Vs ratio near the E2 location (Figure 3 (c, d)) (Nakajima, 2022), likely influence the source of E2. Yoshida et al. (2024) suggested that the foreshock triggered the mainshock through the upward migration of fluids, while Ma et al. (2024) suggested that this earthquake sequence began with a slow rupture in a fluid-rich zone, followed by a faster rupture in a drier region. This sequence may be represented in our BP images: i.e., E1 associated with the initial slow rupture, transitioning to the more rapid rupture propagation of E3 and E4, directed to the west and east, respectively (Figures 3 and 5). The high-frequency event E2 appears to mark the transition from E1 to the subsequent rapid propagation in E3 and E4 (Figures 3, 4, and 5), acting as a bridge for the abrupt change in rupture speed. While such a transition may occur without elevated pore pressure conditions (e.g., Bruhat et al., 2016), crustal fluids may facilitate the effective acceleration of the rupture front (Pampillón et al., 2023). Consequently, the higher-frequency radiation of E2 may result from a combination of abrupt rupture speed changes due to upward-migrating fluids and the initiation of the secondary event in the doublet earthquakes.

Although the complexity of fault geometry may also play a role (MEXT, 2013; Yoshida et al., 2024; Okuwaki et al., 2024), the lack of high-frequency P-wave radiation during E3 and E4 (except for a minor emission at the end of E4) may indicate limited influence from the complex fault network or heterogeneities such as fault barriers.

4.3. E4′: Stopping phase of E4

The fourth high-frequency emission event (E4′ in Figures 3 (d) and 5 (d)) likely represents the stopping phase of fault rupture in the northeastern offshore area of the Noto Peninsula, coinciding with the location of the offshore fault N2 (MEXT, 2013) shown in Figure 1. Classical studies have shown that abrupt rupture termination can effectively generate high-frequency seismic energy (Savage, 1965; Madariaga, 1977). Fault slip models by Fujii and Satake (2024) and Mizutani et al. (2024), based on geodetic and tsunami waveform data, suggested that the northeastern offshore fault N2 did not slip. Besides, seismic waveform inversions including the near-field data (Ma et al., 2024; Xu et al., 2024) found minimal slip on the northeastern offshore fault patch. These observations agree well with our results, which indicate a stopping phase at the northeastern end of the source region near the N2 fault.

4.4. Frequency-dependent P-wave radiation and complex fault rupture process

The low-frequency BP image (0.03-0.5 Hz) reveals the large-scale rupture process, which is consistent with other results of seismic waveform inversions (Okuwaki et al., 2024; Kutschera et al., 2024; Ma et al., 2024; Xu et al., 2024), indicating the bilateral rupture from the hypocentral location. Unlike these previous studies, our multi-frequency BP approach uncovers complex frequency-dependent characteristics in P-wave radiation from the complicated rupture process of multiple fault segments. The most prominent P-wave radiation observed in this study occurs in the lowest-frequency range (0.03–0.3 Hz) in the inland regions of this peninsula (E3), and another notable low- to intermediate-frequency (0.05–0.5 Hz) radiation mainly originates from the northeastern offshore region (E4) (Figure 3 (a, b)). Note that intense high-frequency components (0.1–2.0 Hz) precede these dominant lower-frequency radiations. In this subsection, we discuss the relationship between these lower- and higher-frequency radiation processes in more detail.

A distinct transition in the frequency components of radiated P-waves from high (0.1–2.0 Hz) to low (0.03–0.5 Hz) frequencies after 18 seconds is clearly shown in Figures 3 and 5. E3 appears to be triggered by the high-frequency emission event E2, transitioning smoothly into an intense low-frequency emission (0.03–0.3 Hz) (Figures 3 and 5). Notably, after this frequency transition, E3 radiates almost no higher-frequency radiation and gradually fades after 40 s (Figures 3 and 5) . This behavior can be attributed to near-surface shallow large slip as inferred from the previous waveform inversions (Okuwaki et al., 2024; Ma et al., 2024; Xu et al., 2024). Fault slips at shallower depths often exhibit longer rise times, as seen in the previous inversion studies of other inland earthquakes (e.g., Ji et al., 2015; Hao et al., 2017). Although the exact depth of the P-wave source remains undetermined due to the lack of depth resolution, the lowest-frequency P-wave radiation in the southwestern inland region persists somewhat longer than in any other areas (Figure 3 and 5). Consequently, E3 may not release intense high-frequency energy due to the relatively low slip rate at shallow depths, while the crustal fluid may contribute to further suppressing the higher-frequency signals.

At the end of E3, relatively higher-frequency energy (0.05–0.5 Hz and 0.1–1.0 Hz) are emitted from the southwestern tip of the peninsula ($E3'$ in Figures 3 and 5), which can be interpreted as the stopping phase of E3. However, this termination does not involve the highest-frequency P-wave, which instead appears in E4. In the recent tomographic model (Nakajima, 2022), an anomalously high Vp/Vs ratio was observed in the southwestern area of the Noto Peninsula. A plausible explanation for this stopping phase without higher-frequency emission could be the fluid-rich conditions in this region (Noda and Lapusta, 2013; Madden et al., 2022).

Meanwhile, from E2 to E4, the frequency components of radiated P-waves evolve continuously. E4 can also be triggered by E2, after which the frequency range of emitted P-waves gradually shifts to lower frequencies (0.05–0.5 Hz) (Figures 3 and 5), possibly reflecting the evolution process of fault rupture propagation. After around 36 s, an opposite transition occurs, with the main frequency range smoothly shifting from low to high frequencies (Figures 3 and 5).

A plausible reason for the frequency transition observed toward the end of E4 can be the fault geometry. As suggested by the JSPJ model (MEXT, 2013), aftershock distribution (JMA, 2024a), and the results by Okuwaki et al. (2024), the source region comprises a complex, multi-segmented fault system. Differences in the strike angles are evident between the southwestern inland and northeastern offshore areas. Comparing the two frequency bands (0.05–0.5 Hz and 0.1–1.0 Hz) visualized in Figure 3 (b, c), we observe that, despite the limited resolution of teleseismic P-wave data, the higher- and lower-frequency P-waves at 40–45 s are radiated from the locations near NT3 and NT4, respectively (Figure 3 (b,c)). NT3 and NT4 have apparently different dipping directions (Figure 1 and MEXT (2013)). This significant frequency transition toward the end of E4 may result from such complex multi-segmented fault geometry.

Thus, the intriguing frequency-dependent P-wave radiation sequence of the Mw 7.5 Noto Peninsula earthquake likely results from the effects of the complex fault network under fluid-rich conditions. The presence of crustal fluid may play a key role in triggering the initial stage of this earthquake

(E1) and the main bilateral rupture process (E3, and E4). The complex fault geometry beneath this area likely contributes to the observed variations in frequency-dependent behavior between E3 and E4, indicating the influence of the fault geometry on the slip and rupture processes during this earthquake.

5. Conclusions

In this study, we performed multi-frequency P-wave back-projection to image the frequency-dependent source radiation process for the Mw 7.5 Noto Peninsula earthquake on January 1st, 2024 (or the doublet earthquake of M_{jma} 5.9 and M_{jma} 7.6). Our main findings on the complex radiation process are summarized in the following points:

1. The main source radiation process of the Mw 7.5 Noto Peninsula earthquake lasted approximately 44 s, which can be divided into four episodes (E1–E4).
2. *Episode 1 (E1, 0–15 s):* The P-wave radiation initiates from the hypocenter, with the intense high-frequency energy preceding the lower-frequency radiation, concentrated mainly in the hypocentral region.
3. *Episode 2 (E2, 15–30 s):* This stage bridges E1 and the subsequent episodes, radiating the most intensive high-frequency P-waves from the hypocentral area. This stage likely represents the initial growth for the larger event in the doublet earthquake sequence.
4. *Episodes 3 and 4 (E3 and E4):* These stages encompass the main rupture process, propagating bilaterally from the hypocentral region

towards the southwestern inland and northeastern offshore areas. The rupture during E4 appears to terminate abruptly at the northeastern fault patch, marked by the high-frequency emission at the end of E4.

5. During E3, the low-frequency signals dominate the P-wave radiation, suggesting a relatively longer rise time for the main rupture propagating towards the southwestern inland region.

6. In the initial half of E4, the frequency range of the P-wave radiation transitions smoothly from low to high frequencies, then reverses to a high-to-low frequency transition in the latter half of E4, likely influenced by the complex fault geometry in the northeastern offshore region.

6. Acknowledgments

All seismograms used in this study are downloaded from the IRIS Data Management Center (https://ds.iris.edu/ds/nodes/dmc/). This study was partly supported by JST SPRING grant number JPMJSP2119 to KT and JSPS KAKENHI grand number 24KJ0294 to KT. We used ObsPy (Beyreuther et al., 2010) for seismic waveform analysis and data acquisition. To generate all the figures in this paper, we used matplotlib (Hunter, 2007), cartopy (Met Office, 2010), Generic Mapping Tools (Wessel et al., 2019), and PyGMT (Uieda et al., 2021). In this study, we employed earthquake catalogs by Global CMT (Dziewonski et al., 1981; Ekström et al., 2012) and JMA (JMA, 2024a). In Figures 1 and 3, we used the JSPJ fault model (MEXT,

2013).

7. Data Availability

All the seismograms used in this study are available from the IRIS Data Management Center (https://ds.iris.edu/ds/nodes/dmc/).

References

Adda-Bedia, M., Madariaga, R., 2008. Seismic Radiation from a Kink on an Antiplane FaultSeismic Radiation from a Kink on an Antiplane Fault. Bulletin of the Seismological Society of America 98, 2291–2302. doi:10.1785/0120080003.

Amezawa, Y., Hiramatsu, Y., Miyakawa, A., Imanishi, K., Otsubo, M., 2023. Long-Living Earthquake Swarm and Intermittent Seismicity in the Northeastern Tip of the Noto Peninsula, Japan. Geophysical Research Letters 50. doi:10.1029/2022gl102670.

Beresnev, I.A., 2017. Factors controlling high-frequency radiation from extended ruptures. Journal of Seismology 21, 1277–1284. doi:10.1007/s10950-017-9660-6.

Bernard, P., Madariaga, R., 1984. High-frequency seismic radiation from a buried circular fault. Geophysical Journal of the Royal Astronomical Society 78, 1–17. doi:10.1111/j.1365-246x.1984.tb06468.x.

Beyreuther, M., Barsch, R., Krischer, L., Megies, T., Behr, Y., Wassermann, J., 2010. ObsPy: A Python Toolbox for Seismology. Seismological Research Letters 81, 530–533. doi:10.1785/gssrl.81.3.530.

Bruhat, L., Fang, Z., Dunham, E.M., 2016. Rupture complexity and the supershear transition on rough faults. Journal of Geophysical Research: Solid Earth 121, 210–224. doi:10.1002/2015jb012512.

Dziewonski, A.M., Chou, T., Woodhouse, J.H., 1981. Determination of earthquake source parameters from waveform data for studies of global and regional seismicity. Journal of Geophysical Research: Solid Earth 86, 2825–2852. doi:10.1029/jb086ib04p02825.

Ekström, G., Nettles, M., Dziewoński, A., 2012. The global CMT project 2004–2010: Centroid-moment tensors for 13,017 earthquakes. Physics of the Earth and Planetary Interiors 200, 1–9. doi:10.1016/j.pepi.2012.04.002.

FDMA, 2024. Information on Noto Peninsula Earthquake. URL: https://www.fdma.go.jp/disaster/info/2024/.

Fujii, Y., Satake, K., 2024. Slip distribution of the 2024 Noto Peninsula earthquake (MJMA 7.6) estimated from tsunami waveforms and GNSS data. Earth, Planets and Space 76, 44. doi:10.1186/s40623-024-01991-z.

Gabriel, A., Ampuero, J., Dalguer, L.A., Mai, P.M., 2012. The transition of dynamic rupture styles in elastic media under velocity-weakening friction. Journal of Geophysical Research: Solid Earth 117. doi:10.1029/2012jb009468.

Hao, J., Ji, C., Yao, Z., 2017. Slip history of the 2016 Mw 7.0 Kumamoto earthquake: Intraplate rupture in complex tectonic environment. Geophysical Research Letters 44, 743–750. doi:10.1002/2016gl071543.

Honda, R., Yukutake, Y., Ito, H., Harada, M., Aketagawa, T., Yoshida, A., Sakai, S., Nakagawa, S., Hirata, N., Obara, K., Kimura, H., 2011. A complex rupture image of the 2011 off the Pacific coast of Tohoku Earthquake revealed by the MeSO-net. Earth, Planets and Space 63, 583–588. doi:10.5047/eps.2011.05.034.

Honda, R., Yukutake, Y., Ito, H., Harada, M., Aketagawa, T., Yoshida, A., Sakai, S., Nakagawa, S., Hirata, N., Obara, K., Matsubara, M., Kimura, H., 2013. Rupture process of the largest aftershock of the M 9 Tohoku-oki earthquake obtained from a back-projection approach using the MeSO-net data. Earth, Planets and Space 65, 917–921. doi:10.5047/eps.2013.01.003.

Hunter, J.D., 2007. Matplotlib: A 2D Graphics Environment. Computing in Science & Engineering 9, 90–95. doi:10.1109/mcse.2007.55.

Imanishi, K., Takeo, M., 1998. Estimates of fault dimensions for small earthquakes using stopping phases. Geophysical Research Letters 25, 2897–2900. doi:10.1029/98gl02185.

Imanishi, K., Takeo, M., 2002. An inversion method to analyze rupture processes of small earthquakes using stopping phases. Journal of Geophysical Research: Solid Earth 107, ESE 2–1–ESE 2–16. doi:10.1029/2001jb000201.

Ishii, M., 2011. High-frequency rupture properties of the Mw 9.0 off the Pacific coast of Tohoku Earthquake. Earth, Planets and Space 63, 18. doi:10.5047/eps.2011.07.009.

Ishii, M., Shearer, P.M., Houston, H., Vidale, J.E., 2005. Extent, duration and speed of the 2004 Sumatra–Andaman earthquake imaged by the Hi-Net array. Nature 435, 933–936. doi:10.1038/nature03675.

Ishii, M., Shearer, P.M., Houston, H., Vidale, J.E., 2007. Teleseismic P wave imaging of the 26 December 2004 Sumatra-Andaman and 28 March 2005 Sumatra earthquake ruptures using the Hi-net array. Journal of Geophysical Research: Solid Earth (1978–2012) 112. doi:10.1029/2006jb004700.

Ji, C., Archuleta, R.J., Twardzik, C., 2015. Rupture history of 2014 Mw 6.0 South Napa earthquake inferred from near-fault strong motion data and its impact to the practice of ground strong motion prediction. Geophysical Research Letters 42, 2149–2156. doi:10.1002/2015gl063335.

JMA, 2024a. JMA Earthquake Catalog. URL: https://www.data.jma.go.jp/eqev/data/sourceprocess/index.html.

JMA, 2024b. The Seismological Bulletin of Japan. URL: https://www.data.jma.go.jp/svd/eqev/data/bulletin/catalog/notes_e.html.

Kehoe, H.L., Kiser, E.D., Okubo, P.G., 2019. The Rupture Process of the 2018 Mw 6.9 Hawaii Earthquake as Imaged by a Genetic Algorithm-Based Back-Projection Technique. Geophysical Research Letters 46, 2467–2474. doi:10.1029/2018gl080397.

Kennett, B.L.N., Engdahl, E.R., Buland, R., 1995. Constraints on seismic velocities in the Earth from traveltimes. Geophysical Journal International 122, 108–124. doi:10.1111/j.1365-246x.1995.tb03540.x.

Kind, R., Yuan, X., 2011. Seismic, Receiver Function Technique, Springer Netherlands, Dordrecht, pp. 1258–1269. URL: https://doi.org/10.1007/978-90-481-8702-7_12, doi:10.1007/978-90-481-8702-7_12.

Kiser, E., Ishii, M., 2013a. Hidden aftershocks of the 2011 Mw 9.0 Tohoku, Japan earthquake imaged with the backprojection method. Journal of Geophysical Research: Solid Earth 118, 5564–5576. doi:10.1002/2013jb010158.

Kiser, E., Ishii, M., 2013b. The 2010 Maule, Chile, Coseismic Gap and Its Relationship to the 25 March 2012 Mw 7.1 Earthquake. Bulletin of the Seismological Society of America 103, 1148–1153. doi:10.1785/0120120209.

Kiser, E., Ishii, M., 2016. Back-Projection Imaging of Earthquakes. Annual Review of Earth and Planetary Sciences 45, 1–29. doi:10.1146/annurev-earth-063016-015801.

Koper, K.D., Hutko, A.R., Lay, T., Ammon, C.J., Kanamori, H., 2011. Frequency-dependent rupture process of the 2011 Mw 9.0 Tohoku Earthquake: Comparison of short-period P wave backprojection images and broadband seismic rupture models. Earth, Planets and Space 63, 16. doi:10.5047/eps.2011.05.026.

Koper, K.D., Hutko, A.R., Lay, T., Sufri, O., 2012. Imaging short-period seismic radiation from the 27 February 2010 Chile (M W 8.8) earthquake by back-projection of P , PP , and PKIKP waves: RUPTURE IMAGING OF 2010 CHILE EARTHQUAKE. Journal of Geophysical Research: Solid Earth 117, n/a–n/a. doi:10.1029/2011jb008576.

Kutschera, F., Jia, Z., Oryan, B., Wong, J.W.C., Fan, W., Gabriel, A., 2024. The Multi-Segment Complexity of the 2024 Mw 7.5 Noto Peninsula Earthquake Governs Tsunami Generation. Geophysical Research Letters 51. doi:10.1029/2024gl109790.

Ma, Z., Zeng, H., Luo, H., Liu, Z., Jiang, Y., Aoki, Y., Wang, W., Itoh, Y., Lyu, M., Cui, Y., Yun, S.H., Hill, E.M., Wei, S., 2024. Slow rupture in a fluid-rich fault zone initiated the 2024 Mw 7.5 Noto earthquake. Science , eado5143doi:10.1126/science.ado5143.

Madariaga, R., 1977. High-frequency radiation from crack (stress drop) models of earthquake faulting. Geophysical Journal of the Royal Astronomical Society 51, 625–651. doi:10.1111/j.1365-246x.1977.tb04211.x.

Madariaga, R., 1983. High frequency radiation from dynamic earthquake fault models. Annales de Geophysique 1, 17–23. URL: http://inis.iaea.org/search/search.aspx?orig_q=RN:14783441.

Madariaga, R., 2003. Radiation from a Finite Reverse Fault in a Half Space. pure and applied geophysics 160, 555–577. doi:10.1007/pl00012550.

Madden, E.H., Ulrich, T., Gabriel, A., 2022. The State of Pore Fluid Pressure and 3-D Megathrust Earthquake Dynamics. Journal of Geophysical Research: Solid Earth 127. doi:10.1029/2021jb023382.

Mai, P.M., Aspiotis, T., Aquib, T.A., Cano, E.V., Castro-Cruz, D., Espindola-Carmona, A., Li, B., Li, X., Liu, J., Matrau, R., Nobile, A., Palgunadi, K.H., Ribot, M., Parisi, L., Suhendi, C., Tang, Y., Yalcin, B., Avşar, U., Klinger, Y., Jónsson, S., 2023. The Destructive Earthquake Doublet of 6 February 2023 in South-Central Türkiye and Northwestern Syria: Initial Observations and Analyses. The Seismic Record 3, 105–115. doi:10.1785/0320230007.

Marty, S., Passelègue, F.X., Aubry, J., Bhat, H.S., Schubnel, A., Madariaga, R., 2019. Origin of High-Frequency Radiation During Laboratory Earthquakes. Geophysical Research Letters 46, 3755–3763. doi:10.1029/2018gl080519, arXiv:1901.01219.

Met Office, 2010. Cartopy: a cartographic python library with a Matplotlib interface. URL: https://scitools.org.uk/cartopy.

MEXT, 2013. Integrated Research Project on Seismic and Tsunami Hazards Around the Sea of Japan. URL: https://www.eri.u-tokyo.ac.jp/project/Japan_Sea/index.html.

Mizutani, A., Adriano, B., Mas, E., Koshimura, S., 2024. Fault Model of the 2024 Noto Peninsula Earthquake Based on Aftershock, Tsunami, and GNSS Data doi:10.21203/rs.3.rs-4167995/v1.

Mizutani, A., Yomogida, K., 2022. Back-projection imaging of a tsunami excitation area with ocean-bottom pressure gauge array data. Journal of Geophysical Research: Oceans doi:10.1029/2022jc018480.

Nakajima, J., 2022. Crustal structure beneath earthquake swarm in the Noto peninsula, Japan. Earth, Planets and Space 74, 160. doi:10.1186/s40623-022-01719-x.

Nishimura, T., Hiramatsu, Y., Ohta, Y., 2023. Episodic transient deformation revealed by the analysis of multiple GNSS networks in the Noto Peninsula, central Japan. Scientific Reports 13, 8381. doi:10.1038/s41598-023-35459-z.

Noda, H., Lapusta, N., 2013. Stable creeping fault segments can become destructive as a result of dynamic weakening. Nature 493, 518–521. doi:10.1038/nature11703.

Okuwaki, R., Kasahara, A., Yagi, Y., Hirano, S., Fukahata, Y., 2018. Back-projection to image slip. Geophysical Journal International 216, 1529–1537. doi:10.1093/gji/ggy505.

Okuwaki, R., Yagi, Y., 2017. Role of geometric barriers in irregular-rupture evolution during the 2008 Wenchuan earthquake. Geophysical Journal International 212, 1657–1664. doi:10.1093/gji/ggx502.

Okuwaki, R., Yagi, Y., Hirano, S., 2014. Relationship between High-frequency Radiation and Asperity Ruptures, Revealed by Hybrid Back-projection with a Non-planar Fault Model. Scientific Reports 4, 7120. doi:10.1038/srep07120.

Okuwaki, R., Yagi, Y., Murakami, A., Fukahata, Y., 2024. A Multiplex Rupture Sequence Under Complex Fault Network Due To Preceding Earthquake Swarms During the 2024 Mw 7.5 Noto Peninsula, Japan, Earthquake. Geophysical Research Letters 51. doi:10.1029/2024gl109224.

Pampillón, P., Santillán, D., Mosquera, J.C., Cueto-Felgueroso, L., 2023. The role of pore fluids in supershear earthquake ruptures. Scientific Reports 13, 398. doi:10.1038/s41598-022-27159-x.

Rost, S., Thomas, C., 2002. ARRAY SEISMOLOGY: METHODS AND APPLICATIONS: ARRAY SEISMOLOGY. Reviews of Geophysics 40, 2–1–2–27. doi:10.1029/2000rg000100.

Savage, J.C., 1965. The stopping phase on seismograms. Bulletin of the Seismological Society of America 55, 47–58. doi:10.1785/bssa0550010047.

Spudich, P., Frazer, L.N., 1984. Use of ray theory to calculate high-frequency radiation from earthquake sources having spatially variable rupture velocity and stress drop. Bulletin of the Seismological Society of America 74, 2061–2082. doi:10.1785/bssa0740062061.

Tarumi, K., Yoshizawa, K., 2023. Eruption sequence of the 2022 Hunga Tonga-Hunga Ha'apai explosion from back-projection of teleseismic P waves. Earth and Planetary Science Letters 602, 117966. doi:10.1016/j.epsl.2022.117966.

Uchide, T., Yao, H., Shearer, P.M., 2013. Spatio-temporal distribution of fault slip and high-frequency radiation of the 2010 El Mayor-Cucapah, Mexico earthquake. Journal of Geophysical Research: Solid Earth 118, 1546–1555. doi:10.1002/jgrb.50144.

Uieda, L., Tian, D., Leong, W.J., Jones, M., Schlitzer, W., Toney, L., Grund, M., Yao, J., Magen, Y., Materna, K., Newton, T., Anant, A., Ziebarth, M., Wessel, P., Quinn, J., 2021. PyGMT: A Python interface for the Generic Mapping Tools URL: https://doi.org/10.5281/zenodo.5607255, doi:10.5281/zenodo.5607255. the development of PyGMT has been supported by NSF grants OCE-1558403 and EAR-1948603.

USGS, 2024. M 7.5 - 2024 Noto Peninsula, Japan Earthquake. URL:

https://earthquake.usgs.gov/earthquakes/eventpage/us6000m0xl/executive.

Vinnik, L., 1977. Detection of waves converted from P to SV in the mantle. Physics of the Earth and Planetary Interiors 15, 39–45. URL: https://www.sciencedirect.com/science/article/pii/0031920177900085, doi:10.1016/0031-9201(77)90008-5.

Wessel, P., Luis, J.F., Uieda, L., Scharroo, R., Wobbe, F., Smith, W.H.F., Tian, D., 2019. The Generic Mapping Tools Version 6. Geochemistry, Geophysics, Geosystems 20, 5556–5564. doi:10.1029/2019gc008515.

Xu, L., Ji, C., Meng, L., Ampuero, J.P., Yunjun, Z., Mohanna, S., Aoki, Y., 2024. Dual-initiation ruptures in the 2024 Noto earthquake encircling a fault asperity at a swarm edge. Science 385, 871–876. doi:10.1126/science.adp0493.

Xu, Y., Koper, K.D., Sufri, O., Zhu, L., Hutko, A.R., 2009. Rupture imaging of the Mw 7.9 12 May 2008 Wenchuan earthquake from back projection of teleseismic P waves. Geochemistry, Geophysics, Geosystems 10, n/a–n/a. doi:10.1029/2008gc002335.

Yagi, Y., Nakao, A., Kasahara, A., 2012. Smooth and rapid slip near the Japan Trench during the 2011 Tohoku-oki earthquake revealed by a hybrid back-projection method. Earth and Planetary Science Letters 355, 94–101. doi:10.1016/j.epsl.2012.08.018.

Yoshida, K., Takagi, R., Fukushima, Y., Ando, R., Ohta, Y., Hiramatsu, Y., 2024. Role of a Hidden Fault in the Early Process of the 2024 Mw7.5 Noto Peninsula Earthquake. Geophysical Research Letters 51. doi:10.1029/2024gl110993.

Yoshida, K., Uchida, N., Matsumoto, Y., Orimo, M., Okada, T., Hirahara, S., Kimura, S., Hino, R., 2023a. Earthquake Data for the 2023 Mw6.2 Suzu Earthquake in the Northeastern Noto Peninsula, Japan URL: https://doi.org/10.5281/zenodo.10019860, doi:10.5281/zenodo.10019860.

Yoshida, K., Uchida, N., Matsumoto, Y., Orimo, M., Okada, T., Hirahara, S., Kimura, S., Hino, R., 2023b. Updip Fluid Flow in the Crust of the Northeastern Noto Peninsula, Japan, Triggered the 2023 Mw 6.2 Suzu Earthquake During Swarm Activity. Geophysical Research Letters 50. doi:10.1029/2023gl106023.

Supplementary Materials for

Frequency-dependent seismic radiation process of the 2024 Noto Peninsula earthquake from teleseismic P-wave back-projection

K. Tarumi[1,*] and K. Yoshizawa[1,2]

[1] Department of Natural History Sciences, Graduate School of Science, Hokkaido University, Sapporo 060-0810, Japan
[2]Department of Earth & Planetary Sciences, Faculty of Science, Hokkaido University, Sapporo 060-0810, Japan.
[*]Corresponding author: tarumi.kotaro.jp@gmail.com

Contents:

- Figures S1–S6.
- Captions of Movie S1.

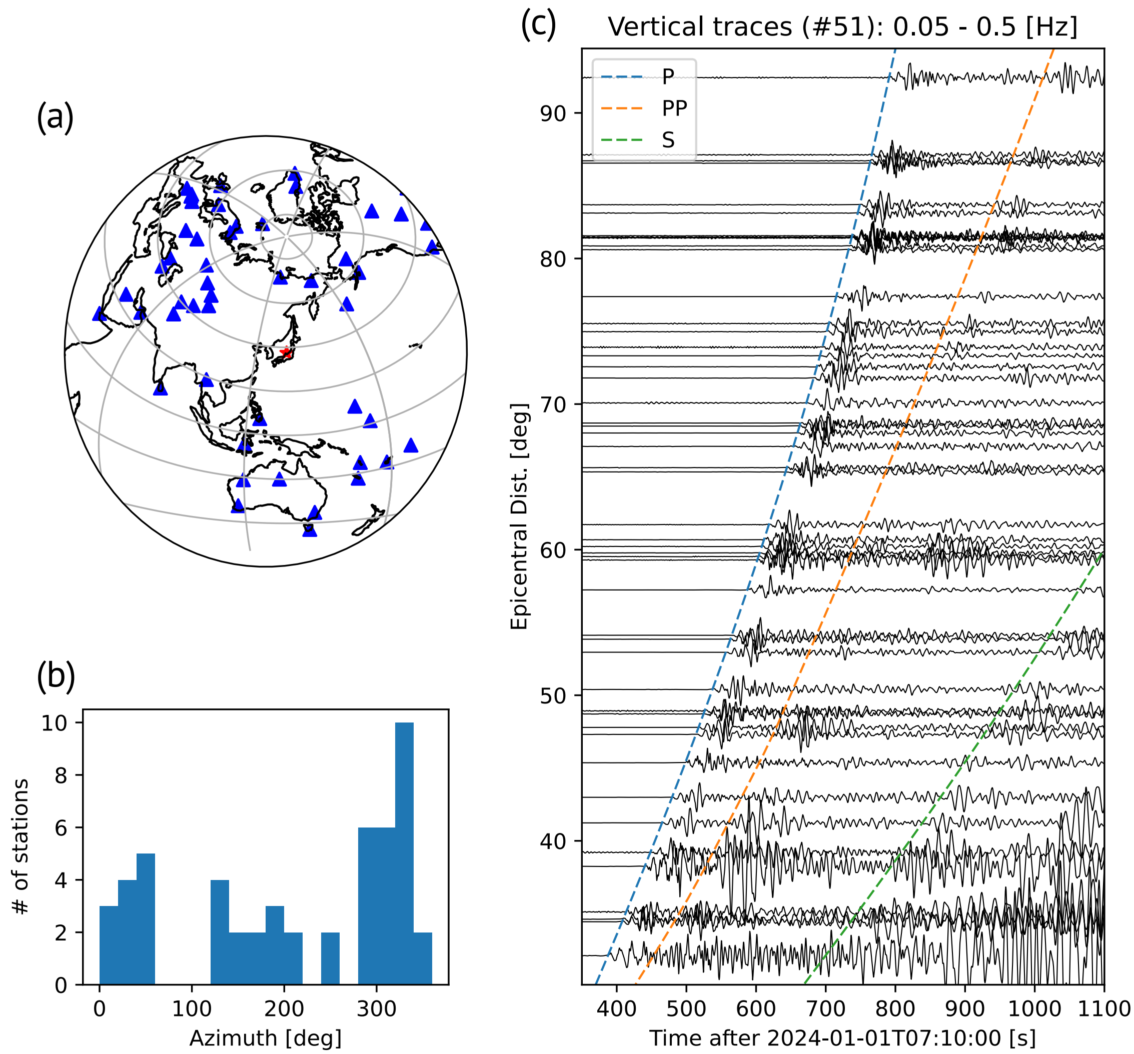

Figure S1. Teleseismic dataset for the frequency range 0.05-0.5 Hz. The figure configuration follows that of Figure 2 in the main text.

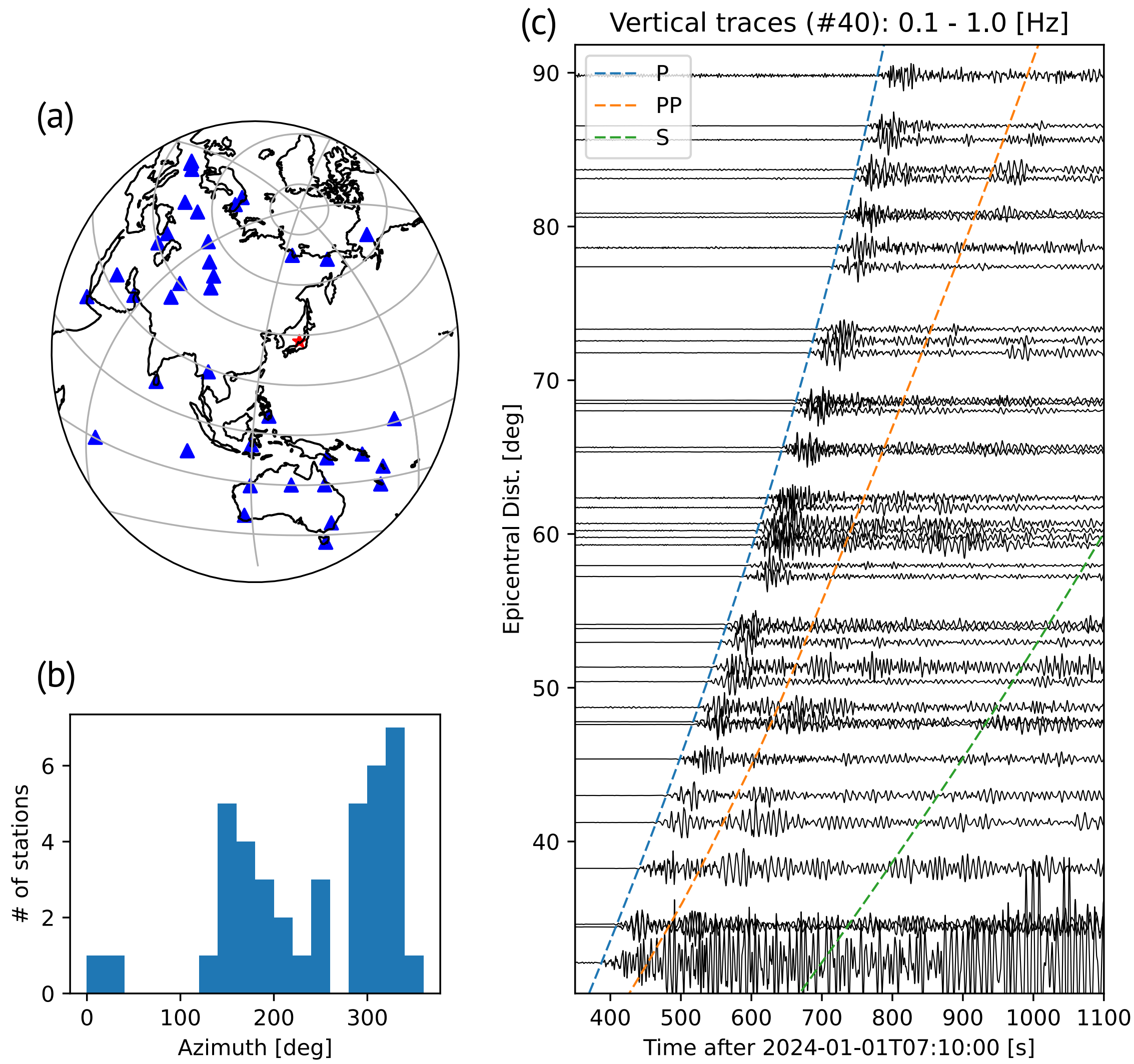

Figure S2: Same as Figure S1, but for 0.1-1.0 Hz.

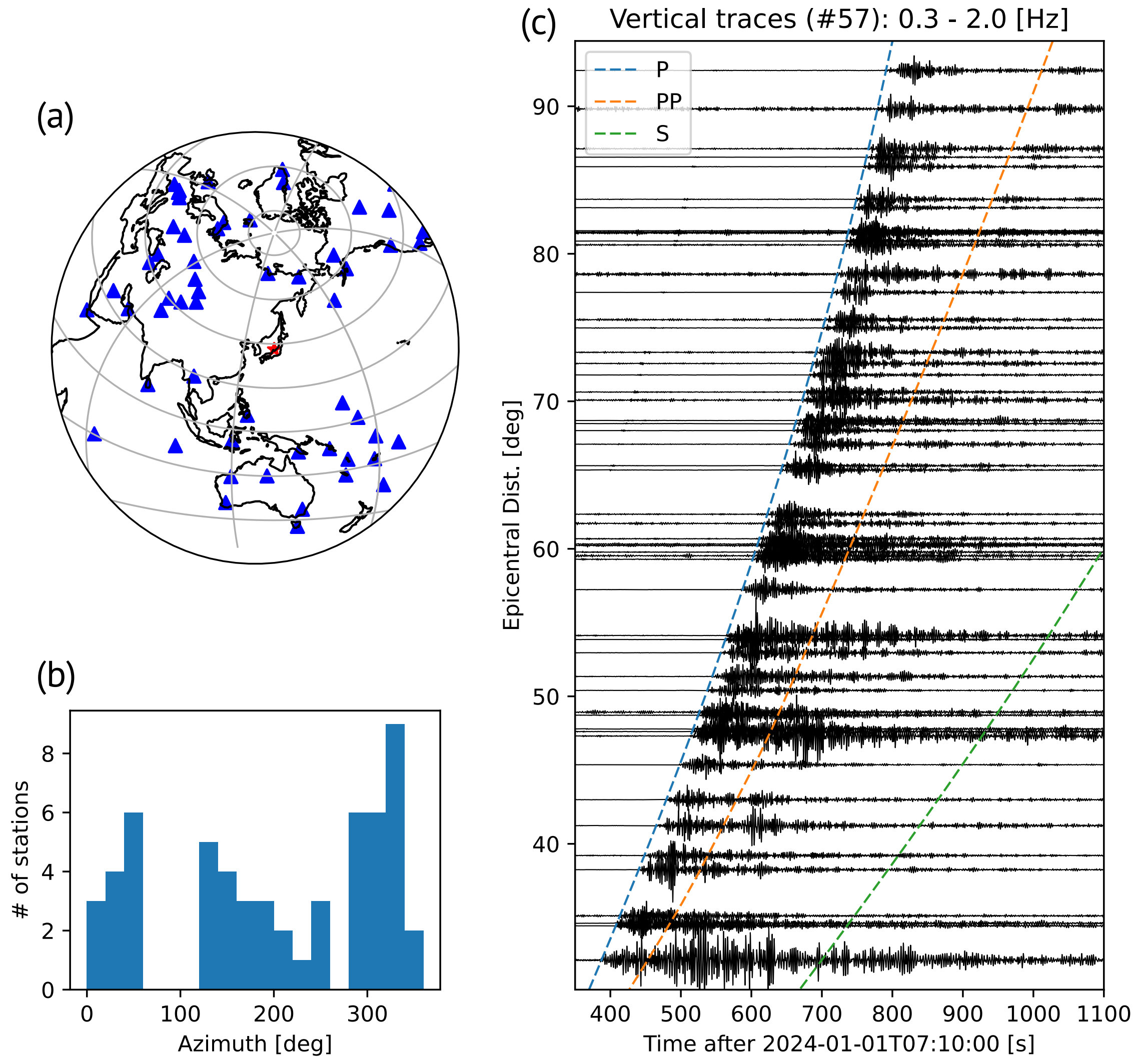

Figure S3: Same as Figure S1, but for 0.3-2.0 Hz.

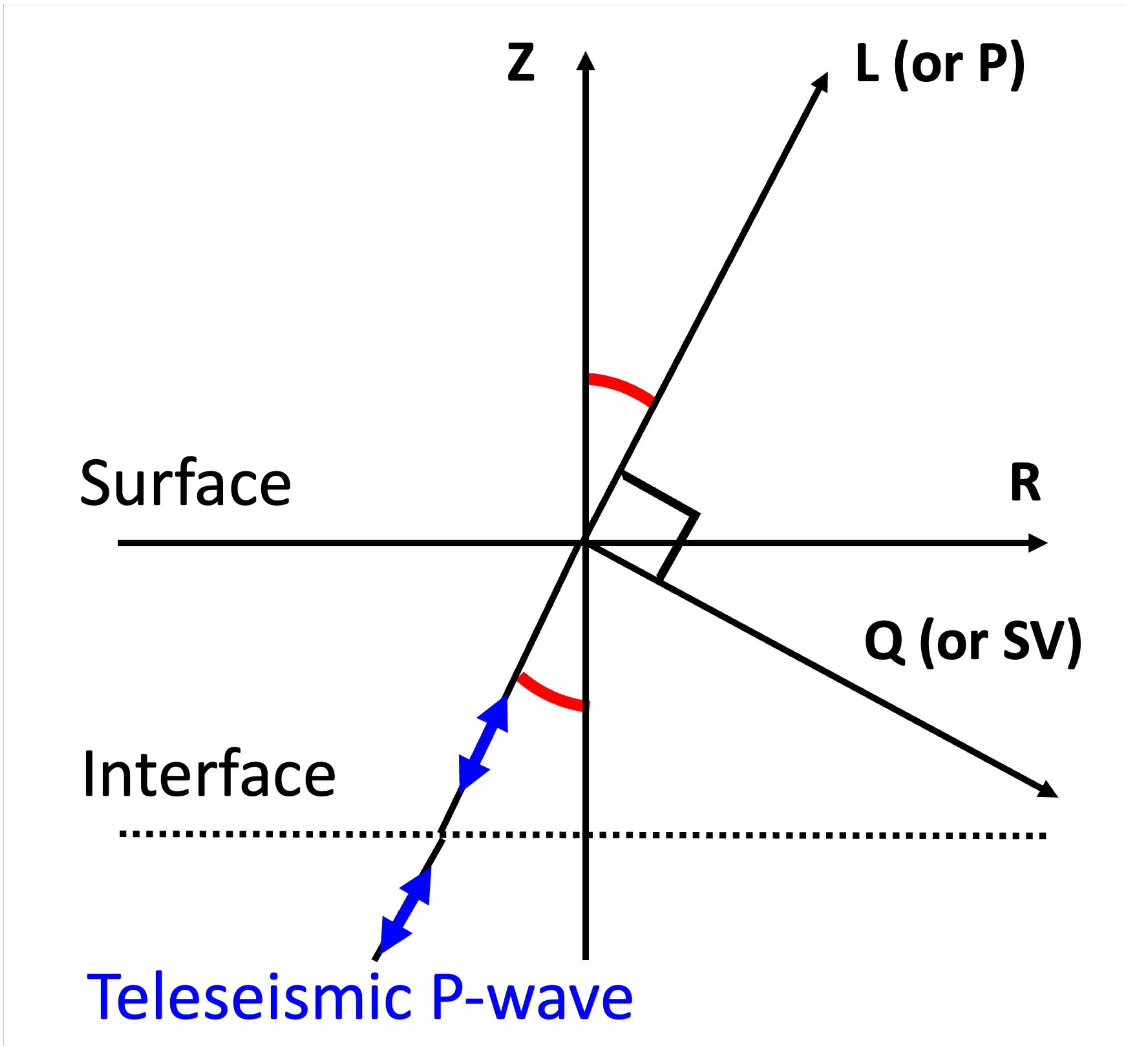

Figure S4: Schematic illustration of the LQT coordinate system at a seismic station.

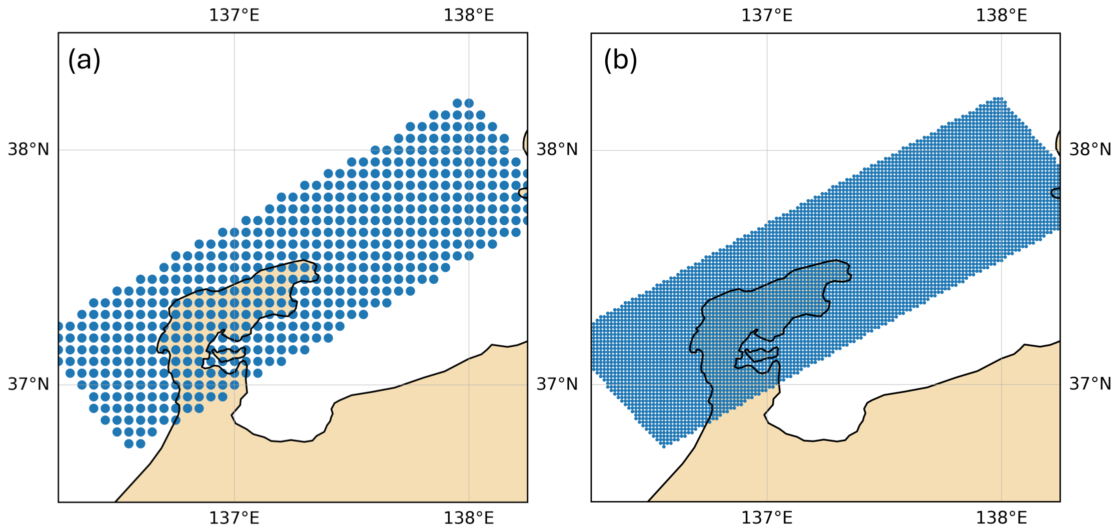

Figure S5: Map view of projected potential source grid points used to generate Figures 5 and S6. (a) 0.05deg girds used for 0.03-0.3, 0.05-0.5, and 0.1-1.0 Hz, (b) 0.015deg used for 0.3-2.0Hz

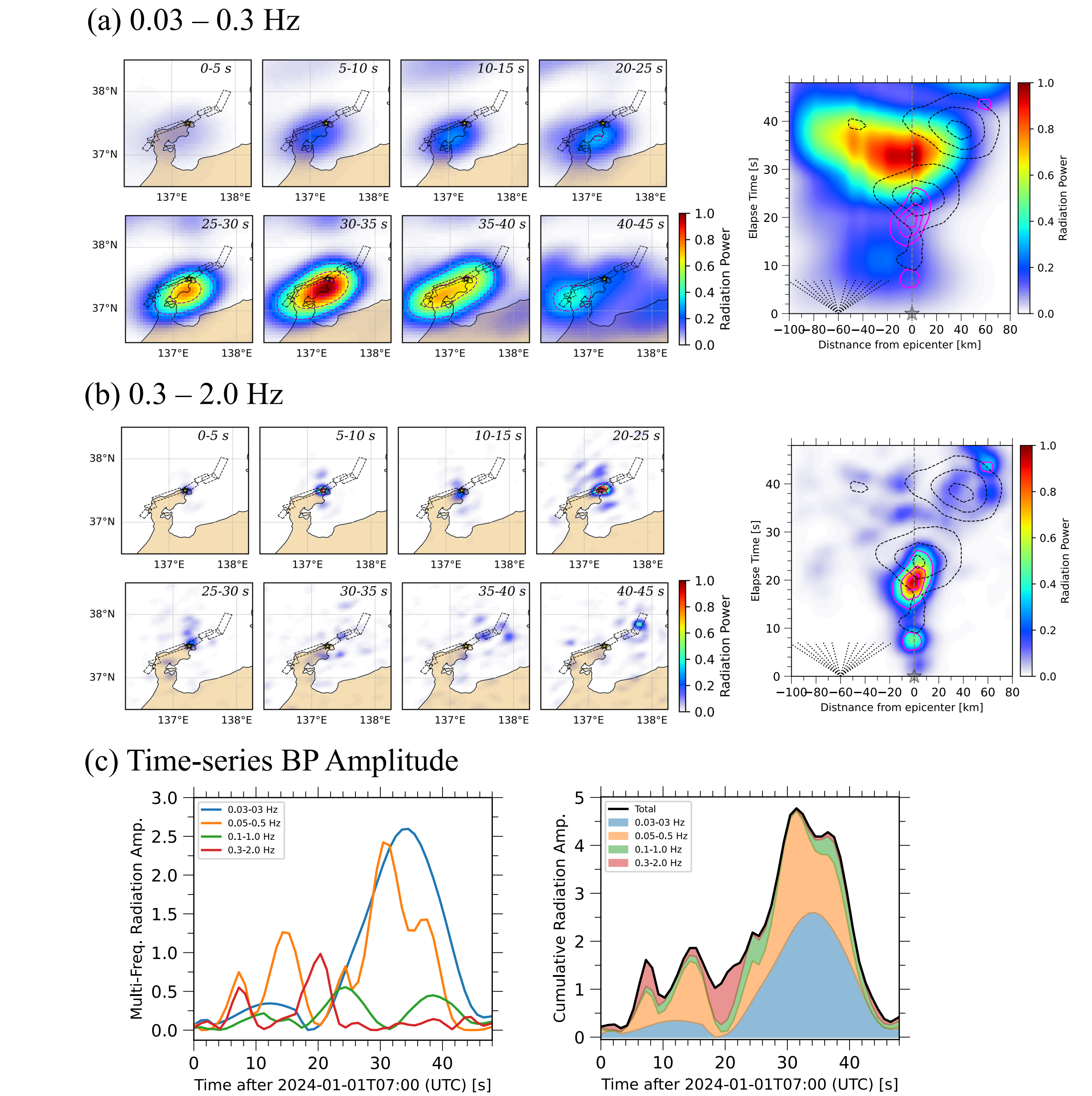

Figure S6: Examples of selected multi-frequency back-projection results using the vertical components without the LQT conversion, following the conventional method. (a, b) Snapshots of BP (left panels) and time-dependent P-wave radiation from the source (right panels), projected along N60Eº, as in Figure 3 but using the conventional BP approach. (c) Same as Figure 4, but for the conventional BP method.

Movie S1: Snapshots of the P-wave back-projection results: (a) 0.03–0.3 Hz, (b) 0.05–0.5 Hz, (c) 0.1–1.0 Hz, and (d) 0.3–2.0 Hz.